Lawrence Berkeley National Laboratory
LBL Publications

Title
In situ electronic characterization of electrochemically tunable metal oxide nanostructures for energy applications via inverted scanning tunneling spectroscopy

Permalink
https://escholarship.org/uc/item/57g6t95w

Journal
Nano Energy, 155

ISSN
2211-2855

Authors
Gallop, Gavin J
McDermott, Ericsson C
Rijal, Puja
et al.

Publication Date
2026-08-01

DOI
10.1016/j.nanoen.2026.112083

Copyright Information
This work is made available under the terms of a Creative Commons Attribution License, available at https://creativecommons.org/licenses/by/4.0/

Peer reviewed

eScholarship.org Powered by the California Digital Library
University of California

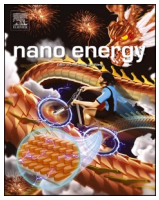
Nano Energy 155 (2026) 112083



Contents lists available at ScienceDirect

Nano Energy

journal homepage: www.elsevier.com/locate/nanoen



Full paper



In situ electronic characterization of electrochemically tunable metal oxide nanostructures for energy applications via inverted scanning tunneling spectroscopy

Gavin J. Gallop [a,1], Ericsson C. McDermott [a], Puja Rijal [a], Alexander C. Kozen [b], A. Alec Talin [c], Janice E. Reutt-Robey [d], Kevin L. Shuford [a], Jonathan M. Larson [a,e,*,1]

[a] Department of Chemistry and Biochemistry, Baylor University, Waco, TX 76798, USA
[b] Department of Physics, University of Vermont, Burlington, VT 05405, USA
[c] Chemistry, Combustion and Materials Science Center, Sandia National Laboratories, Livermore, CA 94550, USA
[d] Department of Chemistry and Biochemistry, University of Maryland, College Park, MD 20742, USA
[e] Energy Technologies and Systems Division, Lawrence Berkeley National Laboratory, Berkeley, CA 94720, USA

ARTICLE INFO

Keywords:
High-aspect-ratio electrochemical nanostructures
Tunneling spectroscopy
Metal-oxide semiconductors
Lithium cobalt oxide / LCO/ $LiCoO_2$
Nanoscale band gap determination
Electrical properties of nano energy materials

ABSTRACT

An *in situ* methodology was developed and implemented to characterize electronic band properties at the apex of high-aspect-ratio nanoscale solid-state electrochemical devices. Model devices with materials relevant to various energy applications were composed of nano-thin metal oxide films coated onto metallic scanning tunneling microscopy (STM) probe tips. Electronic properties of these films at the device apex were measured by inverting the tunneling spectroscopy paradigm: vacuum tunneling spectroscopy between functionalized STM probe tips with ambiguous electronic properties and metallic substrates – a method we here introduce as inverted scanning tunneling spectroscopy (I-STS). Additionally, concentration of metal species within the apex of these metal-oxide devices can be controlled through nanoscale solid-state electrochemistry within the same experimental platform, allowing subsequent *in situ* I-STS measurements that directly reveal how electronic properties change with composition. We first demonstrated and validated the I-STS approach by quantifying the bandgap of nano-thin aluminum oxide (*ca.* 7.1 eV). Next, bandgaps (or lack thereof) of nano-thin stoichiometric lithium cobalt oxide (LCO, *ca.* 1.6 eV) and deeply sub-stoichiometric LCO (0 eV) were observed, directly measuring LCO band evolution along its delithiation-induced semiconductor-to-metal transition. I-STS reveals bandgaps at the nanoscale apex that are substantially narrower than bulk values, demonstrating pronounced modulation of electronic structure in electrochemically active oxide nanostructure termini. Ultimately, I-STS uniquely enables electrical characterization of small, high-aspect-ratio model devices at their apex – a spatial regime inaccessible with existing techniques – and provides a pathway to explore ion-coupled electronic phenomena in advanced energy storage and low-power neuromorphic computing devices using standard STM instrumentation.

1. Introduction

Nano- and/or micro-scale high-aspect-ratio (HAR) structures are frequently used to realize specialized and advanced technologies. Sometimes just a single such structure is used, as is the case for some novel photodetectors [1], electrochemical devices [2], gas sensors [3,4], spectrometers [5], transistors [6–8], and characterization tools [9]. In other cases, small HAR structures are grouped into an ensemble, and a concert-like interaction within the group enables a scientific and/or technological breakthrough. Examples include high performance battery electrodes [10–13], techniques for sensing and imaging pressure distributions [14], devices for sensing and stimulating mammalian neuronal activity [15], energy efficient computing [16], and technologies for scavenging energy from body movements [17]. These nanostructures are incorporated in a variety of ways due to several favorable characteristics that emerge from their small sizes. Fig. 1 illustrates how HAR metal oxide nanostructures are incorporated into various technologies to advance performance. Some novel battery components

* Corresponding author at: Department of Chemistry and Biochemistry, Baylor University, Waco, TX 76798, USA.
E-mail address: jonathan_larson@baylor.edu (J.M. Larson).
[1] These authors contributed equally.

https://doi.org/10.1016/j.nanoen.2026.112083
Received 28 February 2026; Received in revised form 18 May 2026; Accepted 31 May 2026
Available online 2 June 2026
2211-2855/© 2026 The Authors. Published by Elsevier Ltd. This is an open access article under the CC BY license (http://creativecommons.org/licenses/by/4.0/).

utilize forests of vertical nanowires as electrodes to alleviate cracking that frequently occurs in planar electrodes upon bending, or to reduce structural failure during electrode expansion upon lithiation in micro-scale batteries [18–22], while others implement metal oxide nanowires [23–25] or nanosheets [26] in pursuit of improved rate performance and capacity. Low-energy electrochemical neuromorphic computing devices implement metal oxide-coated nanowires to protect wires from oxidation and modulate electronic properties [16], or metal oxide nanowires as transistor-based synapses for their excellent optoelectronic properties [27–29]. HAR metal oxide structures are also of significant interest in other efficient computing architectures, where HAR nanosheet [30] and nanowire [6–8,29] semiconductor transistors are becoming increasingly prevalent. Other relevant applications, such as catalysis [31–33], water splitting [34–37], and solar cells [38,39] take advantage of the unique surface area-to-volume ratios inherent to these nanowire or nanotube geometries, leading to short diffusion distances and promoting efficient chemical conversions.

Regardless of whether one or many small HAR structures are used within a given technology, the physicochemical characterization of a single base structure is key to unveiling fundamental information about the system. Acquisition of such data is essential to expedite informed and strategic engineering-based optimization efforts. In many modern energy and computational technologies, electronic properties are critical to device function and performance. Traditionally, four point or needle probe measurements are used to characterize a material's electronic properties [40], but at the nanoscale these types of measurements are not readily accessible. Alternative methods are available, but are also limited in their utility. The electronic and transport characterization of individual HAR nanostructures typically involves their dispersion onto an insulating substrate, followed by lithographic definition of contact electrodes. Though this is adequate for probing electronic properties along the length of the HAR nanostructures, the quasi-one dimensional apices typically end up buried by contact metal [41]. Alternatively, *in situ* probing using micromanipulators retrofitted in a scanning electron microscope (SEM) can reveal some insights regarding the apex of the HAR nanostructure, but the interpretation of the results can be significantly complicated due to the convolution of the changing properties at the nanoprobe tip [42]. Examples of these methods are shown in Fig. 2a-c. Note that all of these methods require physical contact with the material of interest, do not measure the sample's electronic density of states, and are extremely limited in their ability to characterize the termini of small HAR geometries. Ultimately, empirical determination of the electronic properties of the termini of HAR small structures is quite challenging.

Another powerful characterization method for electronic properties at the nanoscale is scanning tunneling microscopy (STM). This technique, unlike those described above, is a non-contact technique capable of directly probing a material's electronic density of states (DOS). In this method, an STM probe is positioned over a sample to measure the local density of states beneath the probe tip. However, a significant challenge arises when attempting to measure HAR devices as described above. Particularly, aligning the STM probe directly above the termini of such

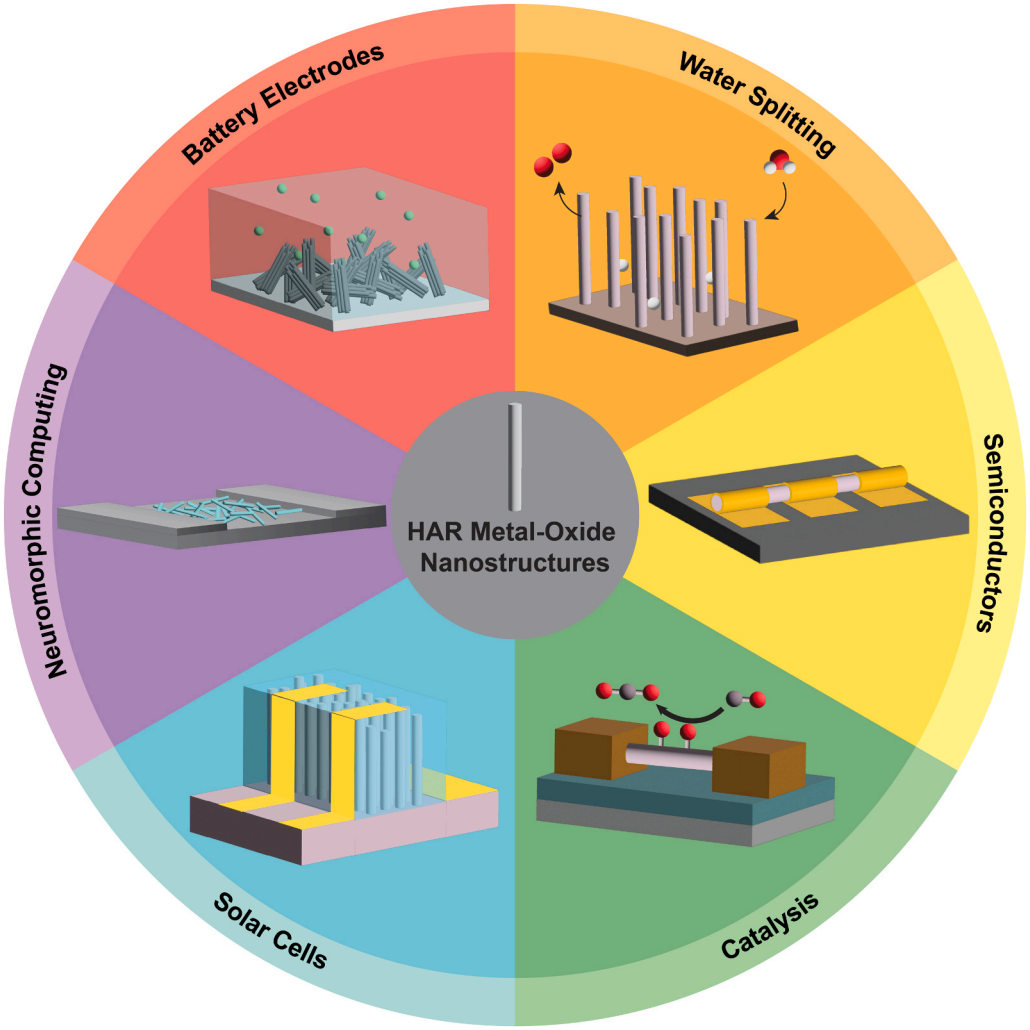


Fig. 1. Renderings of wide-ranging implementations of HAR nanostructures in a variety of technological applications described in the literature.

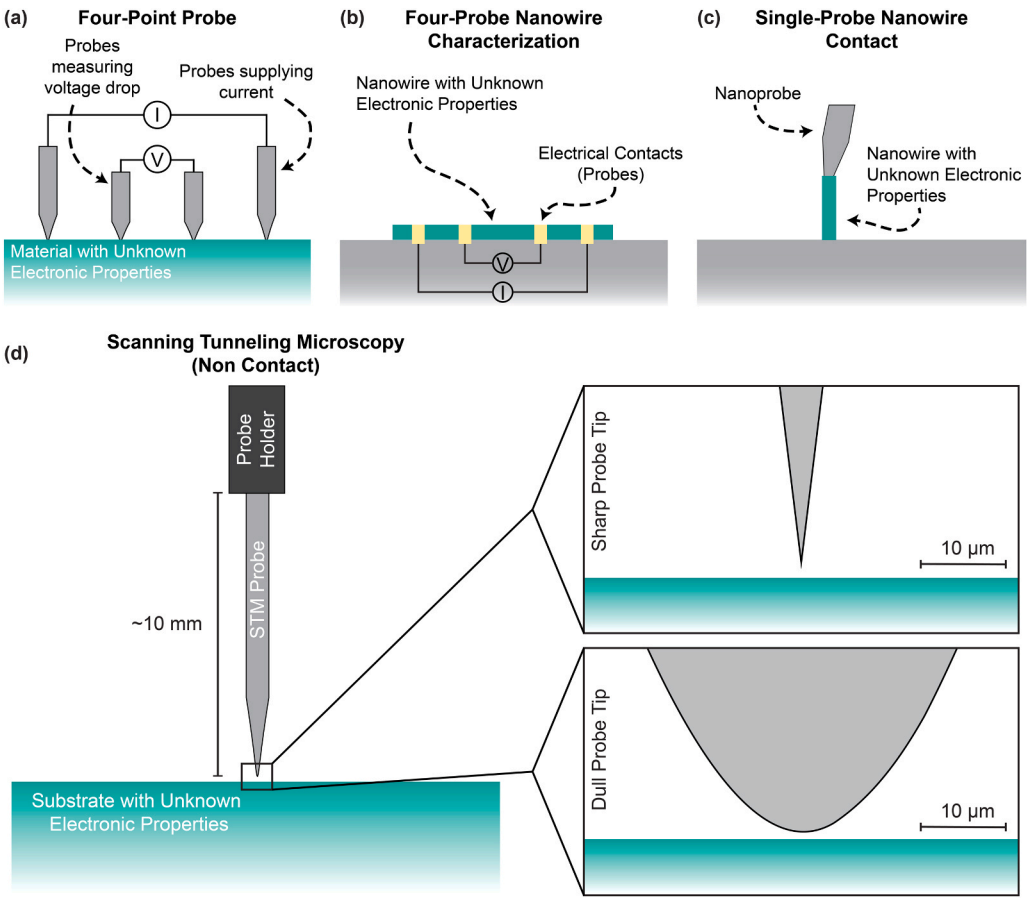


Fig. 2. Typical methods for electronic materials characterization. a) Four-point probe characterization – four probes are brought into contact with the sample, typically a bulk or thin film. A current is applied by the outer probes while the inner probes measure the voltage drop across the material. b) A modified four-point probe method where the micromanipulators are replaced by fixed electrical contacts, for conductivity characterization along the long end of a nanowire. c) A single probe characterization method – a micromanipulator probe is brought into physical contact with the terminus of a nanowire on a substrate to measure the nanowire's conductance along the length of the structure. d) Traditional scanning tunneling spectroscopy setup illustrating the HAR nature of a typical STM probe and the tunability of the probe's radius of curvature from nanometers to microns. Once in the tunneling mode, the tip-sample separation distance is on the order of several angstroms. This is a non-contact electronic characterization method.

nanostructures is exceedingly difficult, and makes traditional scanning tunneling spectroscopy infeasible for this application. In this work, we develop and demonstrate an STM-based approach to address this electrical characterization need. An STM probe is a small HAR structure by construction, with a shank length on the order of several millimeters and a tip apex radius of curvature on the order of tens of nanometers (Fig. 2d). The magnitude of the radius of curvature can further be altered through sharpening or dulling techniques. This enables us to tune the geometries of these probes for use in model devices. We leverage these characteristics to investigate the electronic properties of materials localized to the functionalized probe's apex, which is analogous to the terminus of a nanowire. We further demonstrate the technique's utility on a model electrochemical device, *in situ*. For context, we start with a brief explanation of scanning tunneling spectroscopy (STS).

2. Background

2.1. Scanning tunneling spectroscopy

Over the past several decades [43,44], STS has been used to study the electrical properties of numerous material surfaces. The STS approach probes a surface's local electronic density of states. From the density of states we can extract several valuable properties, including semiconducting band gaps [45–47], superconducting gaps [48,49], conductance plateaus [50], and Urbach energies [51], among several others. While detailed information on the physics [52–55] and broad impact [56–61] of STS can be found elsewhere, we provide here a brief explanation of (i) the technical implementation with working principle and (ii) the data processing scheme and significance of the method.

2.1.1. Technical implementation and working principle

STS is typically implemented by positioning a metallic probe adjacent to a sample with generally unknown electronic properties, in ultrahigh vacuum (UHV) and under bias control, as illustrated in Fig. 3a. When bias is applied to the system and the separation distance (d in Fig. 3b) between the tip and the sample is ideal, typically at the angstrom range, non-negligible wavefunction overlap occurs and electron tunneling between the two bodies becomes possible. STS is then realized by recording the tunneling current, $I(V)$, as the bias is swept across a desired range of values. Because electronic tunneling will only occur when energetically allowed, and because the metallic probe has a smoothly and slowly varying electronic DOS at its Fermi level, the structure of $I(V)$ is dominated by how much, or how little, the sample's local density of states (LDOS) allows tunneling for a given bias. Thus, encoded within the $I(V)$ spectrum is information about the sample's LDOS, ρ_s. This in turn is commonly extracted or approximated with data processing, as we will now describe.

2.1.2. Data processing and significance

The most rudimentary approximation to the sample's LDOS is the

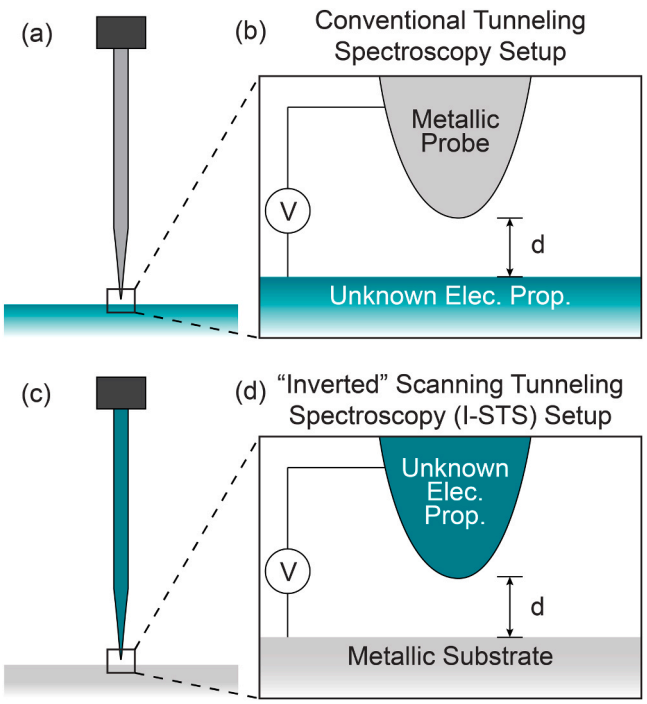


Fig. 3. Schematic cross sections of (a,b) conventional scanning tunneling spectroscopy and (c,d) inverted scanning tunneling spectroscopy.

differential conductance, dI/dV [44]. This can be improved upon by suppressing a voltage dependent background with a straightforward normalization process: taking a ratio of differential conductance to conductance, $(dI/dV)/(I/V)$ [62–65]. However, for surfaces with a gap in their LDOS, this expression may diverge near or within the gap if the conductance approaches zero more quickly than the differential conductance [66]. To circumvent this challenge, a few mathematical schemes to "broaden" the I/V term have been developed [47,66–68]. While the approaches are slightly different from one another in terms of practical implementation, they share a common aim and effect: preventing $(dI/dV)/(I/V)$ from diverging by ensuring that the conductance never vanishes. In this work we adopt one such method [47,67,68] by simply adding a constant, ϵ, to the conductance, giving a final normalized differential conductance of

$$\overline{dI/dV} \equiv \frac{dI/dV}{I/V + \epsilon} \approx \rho_s. \tag{1}$$

Eq. (1) is significant, as it directly relates the processed tunneling spectrum to the sample's LDOS, ρ_s. In our implementation, we varied the value of ϵ across several orders of magnitude to determine the value that provided the most consistent data without suppressing the signal, resulting in a value of $\epsilon = 0.2\,\Omega^{-1}$.

2.2. Inversion of the scanning tunneling spectroscopy paradigm

Before moving on, we pause to highlight a relevant characteristic of this technique that is not immediately apparent from the above discussion. That is, the DOS of the tip and the DOS of the sample enter into the derivation of Eq. (1) in a completely interchangeable way [69]. Thus, if the conventional STS tip and sample materials are exchanged, as depicted in Fig. 3c and 3d, $\overline{dI/dV}$ would approximate the LDOS of the tip's apex, ρ_t, in the same way that traditional STS elicits the LDOS of the substrate. We term such an exchange of materials and subsequent implementation *inverted scanning tunneling spectroscopy* (I-STS).

3. Implementation of inverted scanning tunneling spectroscopy

3.1. Al_2O_3-coated probe tip – materials and methods

For the initial test and demonstration of I-STS, we chose a gold metallic substrate (Fig. 3d). For the small HAR structure of interest with "unknown" electronic properties, we chose a W STM probe tip with approximate radius of curvature (ROC) of 45 nm, coated with a thin film (*ca.* 15 nm) of aluminum oxide (Al_2O_3, alumina) deposited via thermal atomic layer deposition (ALD) using trimethyl aluminum (TMA) and H_2O chemical precursors in a *Cambridge Nanotech Fiji F200 reactor*. Alumina was chosen for its well-studied band gap from the bulk [70–72] to monolayer [73] regimes, and because ALD of alumina not only allows for fine control over film thickness, but is also shown to result in conformal coating on high aspect ratio nanoscale structures [74,75]. It was also chosen due to its importance in a variety of established and emerging electronic devices based on the Josephson Junction [76] and the broad utility thin alumina coatings have developed in energy storage technologies and materials to optimize performance, including reduced interfacial impedance in solid-state batteries [77], increased coulombic efficiency and cycle stability in Li-ion [78,79] and solid-state [80] batteries, and increased reversible capacity in Li-ion batteries [81]. Representative scanning electron microscopy (SEM) and energy dispersive X-ray spectroscopy (EDS) data of the Al_2O_3-coated probe wall are shown in Fig. 4 to convey the uniform coverage of the thin film. Cross-sectional schematics of the combined tip-sample system are shown in Fig. 5a for various tip-sample separations, which are controlled by initial set-point tunneling currents.

The gold substrate and alumina-coated tungsten tip were transferred into a JEOL JSPM−4500A UHV STM system for implementation of I-STS. Bias was applied to the sample with respect to the probe, such that currents at positive bias are associated with electron tunneling from the tip apex to the substrate. Likewise, currents at a negative bias are associated with electron tunneling from the substrate to the tip apex. As the vacuum gap has a resistance orders of magnitude greater than both the contact resistance between the metal probe and oxide coating, and the oxide itself, the vast majority of the voltage drop is expected to occur within the vacuum region, a typical expectation in standard STS measurements [54,65,69]. In tunneling measurements such as these, it is possible to arrive at a fictitiously large band gap if/when tip-sample separation distance, d, is large [82]. To avoid this error, we collected

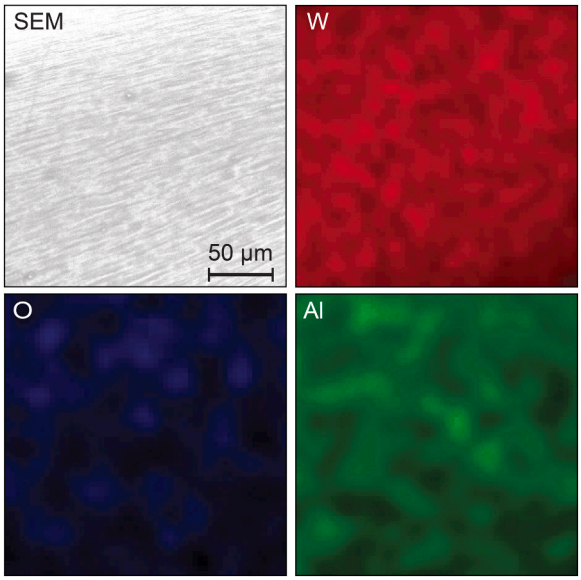


Fig. 4. SEM and EDS data of the Al_2O_3-coated tungsten STM probe tip, showing representative coverage of the probe by the deposited oxide.

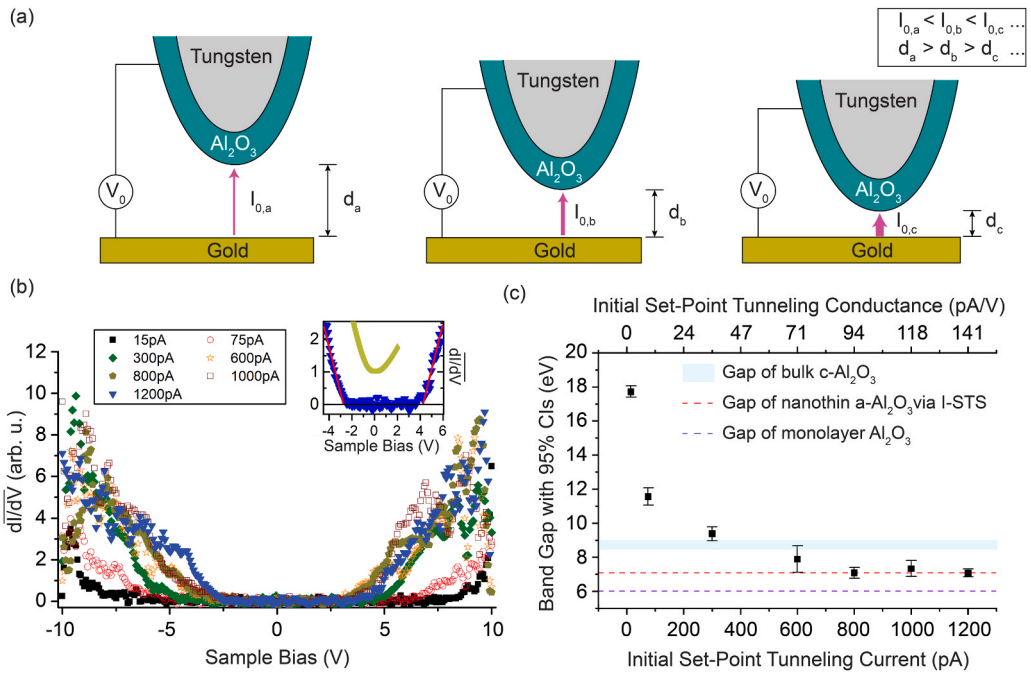


Fig. 5. (a) Schematic cross-sections of the I-STS protocol for an alumina-coated W probe tip adjacent to a gold sample at three different initial set-points ($I_{0,a}$, $I_{0,b}$, $I_{0,c}$…). The direction and thickness of the magenta arrows illustrate the direction and relative amount of initial electron tunneling, respectively. (b) Normalized differential conductance data from I-STS measurements of the alumina-coated probe tip at varying initial set-point tunneling currents and tip-sample separation distances. The inset displays the limiting data, I_0= 1200pA, in blue upside-down triangles, along with red linear fits of the data bounding the gap region. Also plotted inset for comparison purposes is I-STS data for a platinum-iridium tip (yellow triangles) exhibiting the absence of a band gap region as expected for metallic materials. (c) Band gap energies extracted from the room temperature I-STS-measured LDOS localized to the apex of the alumina-coated probe at varying initial set-point currents (black boxes). These approach a limiting value of 7.07 ± 0.24 eV, obtained from the measured gap at 1200 pA and represented by the red dashed line. Also shown are the range of band gap values at room temperature for bulk crystalline alumina reported in the literature (blue band) and the reported theoretical band gap value for monolayer alumina at absolute zero (purple dashed line).

several I-STS measurements with decreasing tip-sample separation distance, to achieve a "limiting" correct gap. This procedure (shown schematically in Fig. 5a) consisted of a series of I-STS measurements (each an average of 20 bias sweeps) over a large "dynamic range" of initial set-point tunneling currents, I_0. The increasing initial set-point tunneling currents spanned three orders of magnitude (15 – 1200 pA, Fig. 5b) as is recommended for clear definition of band edges [83]. All measurements shared a fixed initial sample bias of −8.5 V. A large bias and low initial set-point current are chosen in order to avoid crashing the tip into the sample upon the first approach.

3.2. I-STS of Al_2O_3-coated probe tip

As I_0 increases (and d decreases) the gap in the normalized spectra (regions where $\overline{dI/dV} \approx 0$) is qualitatively observed to shrink before reaching a limiting value. The inset in Fig. 5b contrasts this kind of behavior observed for the alumina-coated tip (I_0 = 1200 pA, blue), with representative data of a metal-vacuum-metal (MVM) tunneling junction: in this case, the normalized differential conductance for a PtIr tip verses gold (yellow triangles, Fig. 5b inset). The choice of PtIr to demonstrate this is arbitrary, as the spectrum for any metal chemistry selected is qualitatively the same. As expected, the normalized differential conductance never vanishes ($\overline{dI/dV} > 0$) – exhibiting the non-vanishing spectrum at zero applied bias – which is the defining characteristic for a MVM tunneling junction and reflects the gapless LDOS and metallic nature of the tip end. We note in passing that $\overline{dI/dV}$ for the MVM junction was produced by application of the normalization steps (Eq. (1)) to a fit of the raw current data (biphasic dose response function; R^2 = 0.999) to prevent numerically-produced outliers arising from numerical differentiation, and division of small numbers near zero applied bias. As for the alumina-coated probe tip (inverted blue triangles, inset 5b), there is a significant voltage window in which $\overline{dI/dV}$ is negligibly small, indicating the presence of a gap in the tip's LDOS, as expected for a wide band gap insulator.

Gap values for each of the Al_2O_3 I-STS measurements were quantified and plotted in Fig. 5c. Determination of each gap value was accomplished by fitting lines to the $\overline{dI/dV}$ data bounding the gap on either side (as shown with red lines in the inset of Fig. 5b), extrapolating the fitted lines to the abscissa, and calculating the absolute value of the difference in abscissa intercepts. Confidence intervals (CIs) of 95% are also plotted and were deduced in a similar way. To calculate the lower bound of the gap CI, a 95% confidence band about the linear fit was used to determine the maximum possible value of the negative-bias intercept, and similarly to determine the minimum possible value of the positive-bias intercept. Then, as before, the absolute value of the difference for these two abscissa intercepts was calculated. The upper bound of the gap CI was calculated in a similarly straightforwardly way, this time by taking the minimum value of the negative-bias intercept and the maximum value of the positive-bias intercept.

Fig. 5c quantitatively illustrates what was qualitatively clear when considering the $\overline{dI/dV}$ data from Fig. 5b. Namely, as the separation distance decreases, the measured gap rapidly decreases, eventually hitting a limiting gap in a somewhat asymptotic manner. We consider the limiting gap value to be the gap which most accurately reflects the tip end's actual LDOS. We then extract ρ_t from the data by an average of the final three measurements, all of which yield strikingly similar values. In this way, via I-STS, we determined the LDOS of a *ca.* 15 nm thick alumina film at the terminus of this HAR structure (an STM probe) to be 7.07 ± 0.24 eV – denoted in Fig. 5c by a red dashed line. Also in Fig. 5c is displayed (i) a blue band highlighting the region of reported room temperature band gaps for bulk crystalline alumina (8.5 – 9 eV) [70–72] and (ii) a purple dashed line at 5.99 eV [73] indicating the theoretical

gap for monolayer Al_2O_3 at absolute zero. Via I-STS, the value for the room temperature band gap of thin-film alumina at the probe apex falls between these two extrema – a reasonable finding for a 15 nm amorphous alumina film. This measured value is in good agreement with reported values for thin films of amorphous alumina in the literature [84,85], further validating the accuracy of this technique.

Out of an abundance of caution, to further ensure the spectra reported above are indeed vacuum tunneling spectra, we next shut off the STM feedback loop for a short time, allowing the piezo to drift and result in physical contact between the probe and the substrate, then collected another I/V spectrum. Upon performing the same measurements following this period, we obtained a gapless Ohmic-like response with significantly greater current than the previous methods, indicating that dielectric breakdown and/or mechanical destruction of the film had occurred. This corroborates that the previous measurements were vacuum tunneling spectra.

4. *In situ* I-STS of a nanoscale electrochemical device

4.1. Nanoscale electrochemical device – materials and methods

So far we have established the motivation, basic theory, implementation steps, feasibility, and reliability of I-STS. We now demonstrate the utility of I-STS for the characterization of the electronic properties of a nanoscale HAR redox active cathode material used primarily in energy storage, as a function of its redox state. We also wanted to explore our ability to implement both sharp and dull tips with the I-STS technique to demonstrate its applicability to a wide range of HAR nanostructure configurations, so for this procedure we dulled the probe tip by electrochemical etching with an aqueous solution of NaOH [65]. The dull probe tip (ROC *ca.* 500 nm) used here also provided greater structural integrity to the device during the delithiation steps outlined in Section 4.3, where the probe tip is brought into physical contact with the substrate. In order to apply this technique *in situ*, we needed to utilize an STM probe apex with the capacity to host and electrochemically dispense Li-ions; such a device was fabricated by sputter-coating the apex of a W STM probe with a 50 nm film of lithium cobalt oxide ($LiCoO_2$, LCO) and annealing at low temperatures (< 260 °C). These protocols for sputter deposition of LCO followed by low-temperature annealing are known in the literature to produce nanocrystalline thin films with the "low-temperature crystalline phase" of LCO (LT-LCO) [86–88]. Representative SEM and EDS data of the LCO coated W STM probe wall are shown in Fig. 6 to confirm coverage.

The selection of materials and device function was guided by the following criteria. First, LCO is a common cathode material in commercialized Li-ion batteries [89,90] and engineering-based optimization pathways requiring basic research will exist for the foreseeable future [91]. Second, LCO has recently been demonstrated to be a promising material in nonvolatile redox transistors for low energy neuromorphic computing [92–96]. Third, the electronic properties of bulk Li_xCoO_2 are empirically known to be extremely sensitive to the amount of Li content – as Li is removed, the band gap is reduced, until it eventually undergoes a semiconductor ($0.95<x\leq1$) to metal ($x<0.75$) phase transition [97–99]. Finally, advanced scanning probe techniques which are involved with or facilitate local nano- or micro- scale electrochemical reactions for basic energy storage science have become increasingly prevalent and impactful [100–111].

In this same vein, we sought a substrate material surface that was amenable to electrochemical lithiation, and which would be metallic both before and after lithiation, so that *in situ* I-STS of the probe apex could be accomplished after electrochemistry. To satisfy these criteria, an oxide-free highly doped Si(100)−2×1 sample was chosen (preparation techniques, including flashing protocols, are in the literature [112,113]), and we experimentally confirmed the 2×1 surface with STM (see Supplementary and Figure S1). This surface was a reasonable candidate because pure Si(100) in the 2×1 reconstruction has a significantly smaller band gap (*ca.* 0.5 eV) [112] than LCO, and once doped heavily, should be metallic. We confirmed this effective metal behavior by performing conventional STS with a W probe. The $\overline{dI/dV}$ spectrum showed the characteristic MVM tunneling junction behavior (Supplementary Figure S2). Further, Si readily hosts Li via electrochemical lithiation and is known to be metallic post-lithiation [114,115]. Additionally, from a materials relevancy perspective, Si is a strong material contender for next-generation anodes [116,117]. In the following, enabled by nanoscale electrochemistry and I-STS, electronic properties of the apex of this HAR model electrochemical device are diagnosed in both a stoichiometric and sub-stochiometric state.

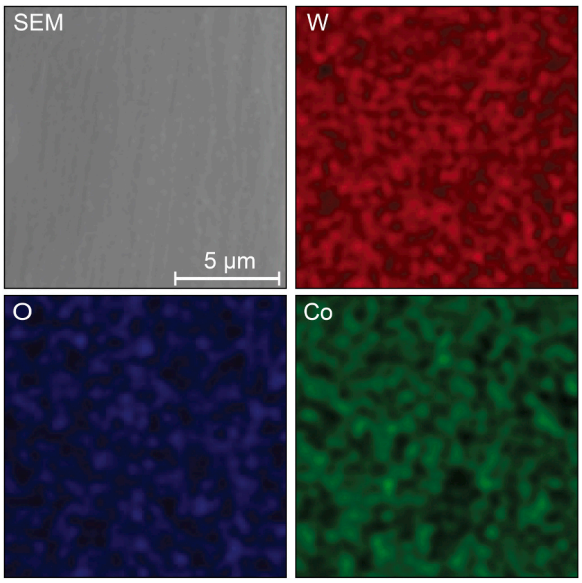


Fig. 6. SEM and EDS mappings of the LCO-coated tungsten STM probe tip. The coverage shown in the Co and O mappings indicate total coverage of the probe tip by the deposited LCO.

4.2. I-STS of stoichiometric LCO probe tip

We first conducted I-STS of the apex of the as-deposited LCO-coated device in a similar manner as described in Section 3. The limiting I-STS measurement configuration is illustrated in Fig. 7a and corresponding normalized differential conductance (average of 20 measurements) is plotted in Fig. 7d. We note that in narrow-gap semiconductors, peaks can present in the $\overline{dI/dV}$ data and define the gap boundaries [51]. This is the case here. Because the bias is applied to the substrate with respect to the probe, as the bias is swept into the negative range electron energies in the substrate rise. Once they reach the available energy states in the tip, tunneling occurs. Similarly, when the bias is swept into the positive range electron energies in the substrate decrease until electrons in the tip's valence band tunnel to the substrate. Thus, the peak at *ca.* −0.83 V corresponds to the onset of the tip's conduction band (CB) while the peak at *ca.* 0.75 V corresponds to the onset of the tip's valence band (VB). Therefore, the as-deposited LCO within the terminus region of the probe tip possesses a measured gap of *ca.* 1.6 eV. Several values have been reported in the literature for the band gap of LCO in various forms. Bulk crystalline LCO is experimentally reported to have a band gap of 2.7 eV [118], while the most recent and robust computational results available suggest a range of *ca.* 2.4 – 2.8 eV [119] (via GGA+U due to the presence of Co – see B. Andriyevsky et al. [119] and Section 4.5). Experimental measurements performed on sputtered nano-thin nanocrystalline films of LCO, deposited using RF sputtering techniques similar to those employed here, result in band gaps from 2.2 to 2.3 eV [120,121]. While our HAR nanostructure was similarly composed of sputtered nano-thin nanocrystalline films of LCO, the I-STS-measured

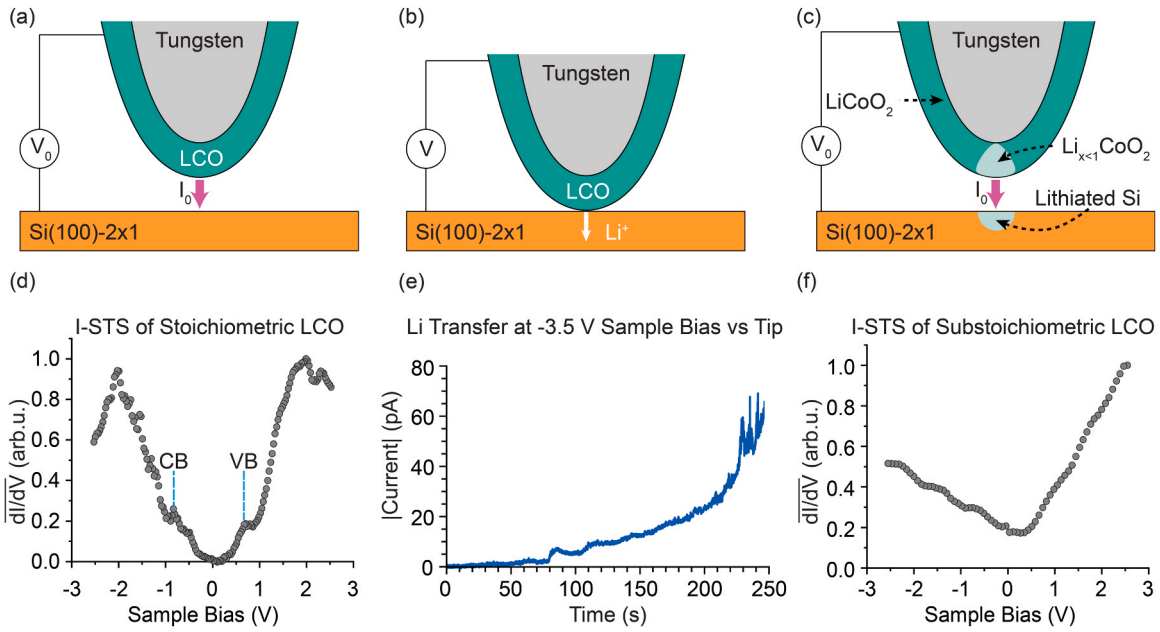


Fig. 7. Schematic illustrations of (a) I-STS characterization of the as-deposited LCO-coated probe vs oxide-free Si(100)−2 × 1, (b) local electrochemical lithiation of the same Si surface via the LCO-coated probe, and (c) I-STS characterization of the sub-stochiometric terminus region of the probe vs the lithiated Si. Below these schematics are the corresponding measurements for each procedure: (d) the I-STS spectrum for the LCO-coated probe apex in the as-deposited state (average of 20 measurements); (e) electrochemical lithiation data showing |current| vs time at −3.5 V applied bias, showing that current increases with time for a fixed bias while the tip is in physical contact with the Si substrate; and (f) the I-STS spectrum for the partially-delithiated LCO-coated probe apex (average of 50 measurements). Spectra are normalized to their max value within the measured bias range.

gap of *ca.* 1.6 eV is notably less than the aforementioned results for planar sputtered thin films. This suggests that the unique local physicochemical characteristics of this confined nanoscale geometry – including extreme curvature, local stress and strain, local large electric fields, surface dangling bonds, and so on – are non-negligibly involved in influencing the electrical properties at the terminus of the metal oxide structure. In fact, the measured gap is closer to the experimentally measured gap of nanocrystalline powder LCO with 51 nm particle size (1.68 eV) [122], further implicating the nanoscale geometry and related coupled local effects.

4.3. Delithiation of LCO probe tip

Next, we performed local electrochemical lithiation of the Si(100)−2 × 1 surface in the following way. While the LCO-coated STM probe tip was held above the surface, a fixed bias of −3.5 V was applied to the Si substrate with respect to the tip. The probe tip was then carefully lowered until it came into contact with the substrate (Fig. 7b) as evidenced by rapid increase in current (more detailed protocols for this process can be found elsewhere in the literature [104,107,108]). Once the tip and surface are in physical contact in the absence of an electrolyte, the applied bias induces both electron and Li-ion transfer between the LCO probe tip apex and the Si surface. During this electrochemistry, the tip-sample separation and applied bias are held constant (0 nm and −3.5 V, respectively) and the current is recorded. Interestingly, even though the sample separation and bias remained constant, the current was observed to increase with time in a non-linear manner, as shown in Fig. 7e. We interpret this as strong evidence that the electron conductivities of both the LCO and Si surfaces were increasing due to (i) a semiconductor-to-metal transition in the LCO brought on by a sufficient removal of Li from the tip apex and (ii) a synchronous increase in Si substrate conductivity brought on by Li intercalation. These hypotheses are next tested *in situ* with sequential I-STS.

4.4. I-STS of sub-stoichiometric LCO probe tip

Following local electrochemical lithiation of the Si(100)−2 × 1 surface with simultaneous delithiation of the LCO probe tip end, the probe was removed from contact and retracted out of tunneling range. I-STS protocols as described above in Section 3 were then again commenced. Fig. 7c depicts a schematic of this measurement and highlights the best understanding of the local materials' qualitative stoichiometry prior to the I-STS measurements. The limiting I-STS results, averaged over 50 measurements, are presented in Fig. 7f. In this spectrum, the lack of any region with vanishing LDOS within the measured voltage range indicates a metal/vacuum/metal tunneling junction, as it did in the case of the PtIr/vacuum/Au case shown in the inset of Fig. 5b. These data thus confirm that both tip end and sample LDOSs are metallic in character. Evidently, during the nanoscale electrochemical lithiation of Si and LCO delithiation, enough Li left the probe tip's end to (i) induce the metal transition in LCO such that $x<0.75$ and (ii) metallicize the Si substrate. Density functional theory (DFT) calculations were conducted over a range of LCO stoichiometries to confirm band gap trends.

4.5. Density functional theory of LCO: from stoichiometric to sub-stoichiometric

Spin-polarized DFT calculations were performed using Vienna Ab initio Simulation Package (VASP) [123,124] within the projector augmented wave (PAW) formalism [125,126], with exchange–correlation described by the Perdew–Burke–Ernzerhof (PBE) functional [127] and on-site Co 3d correlations treated via the Dudarev generalized gradient approximation plus Hubbard U (GGA+*U*) approach [128]. Two Hubbard parameters, U = 3.3 eV [129,130] and U = 4.9 eV [131], were employed to assess sensitivity of the computed gaps to this choice, both having precedent in the LCO literature. Li_xCoO_2 structures were modeled using a 2 × 2 × 1 supercell across a range of Li concentrations spanning the full delithiation regime, with sub-stoichiometric compositions generated by systematic removal of Li atoms from

interlayer sites. Crystal structures were visualized using Visualization for Electronic and Structural Analysis (VESTA) [132], and representative relaxed structures at x = 1.0, 0.5, and 0.25 are shown in Fig. 8(a), illustrating that the layered cobalt–oxygen framework is preserved across all compositions while interlayer spacing evolves with Li content. Importantly, these calculations model the single-crystalline phase of Li_xCoO_2, whereas the sputter-deposited film characterized via I-STS is expected to be nanocrystalline. This is a key distinction to keep in mind when comparing computed and measured gap values.

The computed band gaps across all Li concentrations for both U values are presented in Fig. 8(b). At full lithiation (x = 1.0), the parameterizations yield clear semiconducting gaps of 2.88 eV (U = 4.9 eV) and 2.12 eV (U = 3.3 eV), consistent with prior reports for crystalline LCO [99,118,120]. The divergence between the two U values at x = 1.0 is expected, as the Hubbard correction most strongly influences the gap when Co 3d electrons are fully localized in the Co^{3+} state. Upon delithiation and development of mixed Co^{3+}/Co^{4+} valence across multiple intermediate compositions, the electronic structure becomes more itinerant and the two parameterizations converge, yielding nearly identical gaps of 1.75 eV and 1.76 eV at x = 0.75. As lithium is further removed, both parameterizations show a dramatic and sustained gap collapse to near-zero values across all computed compositions for x < 0.75, in direct agreement with the experimentally established semiconductor-to-metal transition boundary in Li_xCoO_2 [97–99].

The I-STS measurements and DFT calculations share the same essential qualitative trend and together present a consistent picture of the delithiation-driven electronic evolution of LCO. Both DFT-calculated values at x = 1.0 nonetheless exceed the I-STS-measured gap of *ca.* 1.6 eV at the probe apex. As these DFT calculations are limited to bulk single-crystal structures and the experimentally-assessed sample is nanocrystalline, we expect to observe this discrepancy. The most critical feature is reproduced by both theory and experiment: beginning from a clear semiconducting gap at full lithiation (x = 1.0), the band gap collapses to near-zero values across all computed compositions for x < 0.75. This agreement underscores that lithium content is the primary driver of electronic structure evolution in Li_xCoO_2, and that I-STS is uniquely positioned to track this evolution *in situ* at the nanoscale.

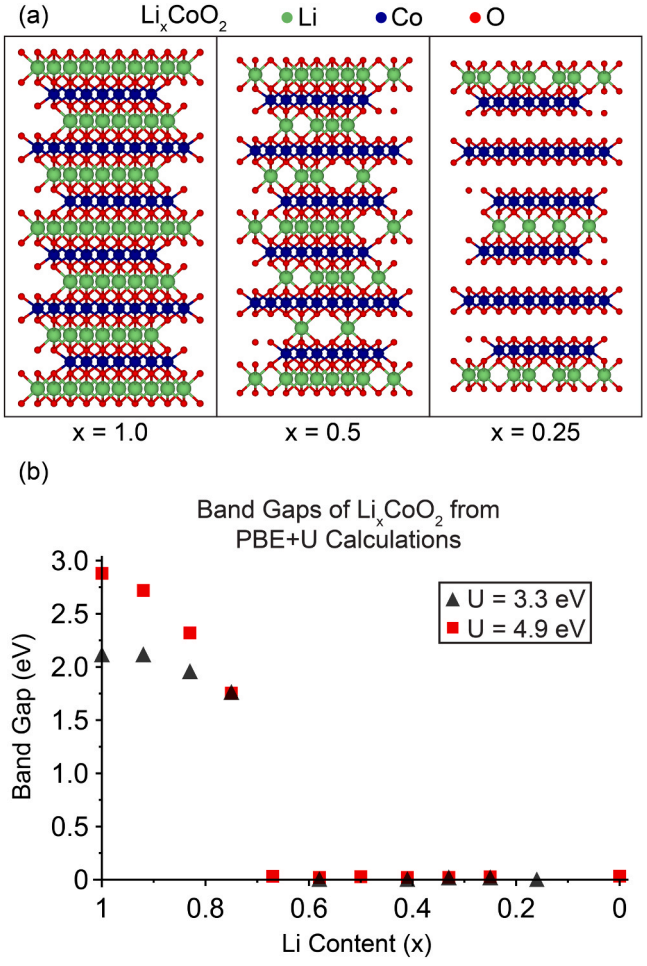


Fig. 8. DFT-computed electronic structure of Li_xCoO_2 as a function of lithium content. (a) Relaxed crystal structures at x = 1.0, 0.5, and 0.25 viewed along the a-axis, with green, blue, and red spheres representing Li, Co, and O atoms, respectively; open sites denote Li vacancies introduced upon delithiation. The layered Co–O framework is preserved across all compositions, with interlayer spacing evolving systematically with Li content. (b) Calculated band gap energies versus Li content for U = 3.3 eV (black triangles) and U = 4.9 eV (red squares) from PBE+U calculations.

5. Discussion and conclusions

These measurements of the LDOS of the apex of STM probe tips clad in nanoscale metal oxide films, coupled with theoretical calculations of these materials, demonstrate that I-STS is a potent tool for highly specialized characterization of HAR micro- to nanoscale structures. The data presented herein show the utility of the I-STS methodology to effectively characterize the termini of model HAR nano- to microscale electrochemical devices while simultaneously altering the devices' chemical compositions, a capability that is exceedingly difficult to achieve through other existing techniques. The feasibility of this method was demonstrated by quantitative determination of the band gap of a thin alumina film, deposited at the apex of an STM probe. The further utility of I-STS for energy materials-related applications was exemplified with *in situ* characterization of the electrical properties of a model LCO-based solid-state electrochemical device at two distinct points along its typical operational pathway. In particular, I-STS was used to track the evolution of the device materials' chemistry via direct measure of the anode/cathode materials' evolving electronic structure upon a change in stoichiometry. Notably, the I-STS protocols presented here are readily accessible via standard scanning tunneling microscopy instrumentation, with the only alteration being the probe-tip cladding, thus further expanding the functionality of an already versatile technology leveraged in nanoscale energy materials science. Beyond the specific applications demonstrated here, ultimately this technique is intended to be highly valuable to a vast range of technologies by providing a novel experimental platform to electrically characterize the termini of a diversity of HAR structures, regardless of geometry or chemistry. For example, characterizing the electrical properties of nanotube termini relevant in energy technologies (we note nanotube attachment to the end of AFM probes has already been reported in the literature [104,133–135]). We note also that this technique could be implemented with a low-temperature UHV STM to investigate low-T device applications, or to obtain clearer band edge definitions by removal of thermally-induced band broadening.

The characterization of the electronic properties of metal oxides found in electrochemical energy storage devices is critical for optimizing these technologies. These devices may incorporate nanostructures or may be nanoscale themselves. Their electronic properties are dependent on both ion concentration and size. I-STS uniquely allows researchers to perform typical electrochemical actions – here demonstrated through Li^+ ion transfer – while measuring the electronic properties that result from controlled material transfer, without the need to alter the experimental setup. These characteristics make I-STS particularly well-suited for *in situ* studies of ion-induced property changes in energy storage materials research. I-STS is also a highly applicable characterization technique in the field of low energy neuromorphic computing, where metal oxides and nanowires are commonly utilized in transistors. Model LCO-based and nanowire transistors can be characterized with I-STS *in situ* while tracking changes in their electrical properties, aiding in the

identification of new materials and structures for device architecture optimization. These applications in both energy storage and low-energy neuromorphic computation demand novel characterization techniques for HAR nanoscale electrochemical devices, which is aptly addressed by I-STS.

Given the combination of accessibility and versatility of this method, this work should have immediate impact on researchers from a diversity of fields interested in performing electrochemical manipulation and characterization of metal oxide nanostructures, and particularly those investigating materials with electrochemically tunable electronic properties. I-STS is an ideal characterization technique for these applications, as it allows for *in situ* electrochemical manipulation of ions and subsequent probing of electronic property changes at the nanoscale using a single experimental system.

CRediT authorship contribution statement

Alexander C. Kozen: Writing – review & editing, Validation, Resources, Investigation. **Puja Rijal:** Writing – review & editing, Writing – original draft, Visualization, Validation, Methodology, Investigation, Formal analysis, Data curation. **Ericsson C. McDermott:** Writing – review & editing, Writing – original draft, Visualization, Validation, Methodology, Investigation, Formal analysis. **Gallop Gavin G.:** Writing – review & editing, Writing – original draft, Visualization, Validation, Methodology, Investigation, Formal analysis. **Jonathan M. Larson:** Writing – review & editing, Writing – original draft, Visualization, Validation, Supervision, Resources, Project administration, Methodology, Investigation, Funding acquisition, Formal analysis, Data curation, Conceptualization. **Kevin L. Shuford:** Writing – review & editing, Validation, Supervision, Resources, Methodology, Funding acquisition. **Janice E. Reutt-Robey:** Writing – review & editing, Visualization, Supervision, Resources, Methodology, Funding acquisition. **A. Alec Talin:** Writing – review & editing, Validation, Resources, Investigation.

Declaration of Competing Interest

The authors declare that they have no known competing financial interests or personal relationships that could have appeared to influence the work reported in this paper.

Acknowledgements

G.J.G., E.C.M., and J.M.L. acknowledge Baylor University for financial support through startup funds.

This work used Stampede3 at Texas Advanced Computing Center (TACC) through allocation MAT250045 from the Advanced Cyberinfrastructure Coordination Ecosystem: Services & Support (ACCESS) program, which is supported by U.S. National Science Foundation grants #2138259, #2138286, #2138307, #2137603, and #2138296 [136]. Support for P.R. and K.L.S. was provided by the National Science Foundation under award number 2147956. The authors also thank Baylor University High Performance Research Computing for computational resources on the Kodiak HPC cluster.

This work was supported by the Nanostructures for Electrical Energy Storage, an Energy Frontier Research Center funded by the U.S. Department of Energy, Office of Science, Office of Basic Energy Sciences under award no. DESC0001160.

A.A.T. was supported by the Sandia Laboratory-Directed Research and Development (LDRD) Program. Sandia National Laboratories is a multimission laboratory managed and operated by National Technology and Engineering Solutions of Sandia, LLC., a wholly owned subsidiary of Honeywell International, Inc., for the US Department of Energy's National Nuclear Security Administration under contract DE-NA−0003525. The views expressed in the article do not necessarily represent the views of the US Department of Energy or the United States Government.

Appendix A. Supporting information

Supplementary data associated with this article can be found in the online version at doi:10.1016/j.nanoen.2026.112083.

Data availability

Data will be made available on request.

References

[1] G.A. O'Brien, A.J. Quinn, D.A. Tanner, G. Redmond, A single polymer nanowire photodetector, Adv. Mater. 18 (2006) 2379–2383, https://doi.org/10.1002/adma.200601012.
[2] L. Mai, Y. Dong, L. Xu, C. Han, Single nanowire electrochemical devices, Nano Lett. 10 (2010) 4273–4278, https://doi.org/10.1021/nl102845r.
[3] F. Hernandez-Ramirez, J.D. Prades, A. Hackner, T. Fischer, G. Mueller, S. Mathur, J.R. Morante, Miniaturized ionization gas sensors from single metal oxide nanowires, Nanoscale 3 (2011) 630–634, https://doi.org/10.1039/c0nr00528b.
[4] M. Tonezzer, N.V. Hieu, Size-dependent response of single-nanowire gas sensors, Sens. Actuators B Chem. 163 (2012) 146–152, https://doi.org/10.1016/j.snb.2012.01.022.
[5] Z. Yang, T. Albrow-Owen, H. Cui, J. Alexander-Webber, F. Gu, X. Wang, T.C. Wu, M. Zhuge, C. Williams, P. Wang, A.V. Zayats, W. Cai, L. Dai, S. Hofmann, M. Overend, L. Tong, Q. Yang, Z. Sun, T. Hasan, Single-nanowire spectrometers, Science 365 (2019) 1017–1020, https://doi.org/10.1126/science.aax8814.
[6] M.D. Cortinhal, A.I.B. Rovisco, P.M.C. Barquinha, One dimensional metal oxide semiconductor nanotransistors, Adv. Mater. Technol. 10 (2025), https://doi.org/10.1002/admt.202500735.
[7] Y. Jeon, S. Kim, Vertical stacking of ZnO nanowire devices with different functionalities on plastic substrates, Phys. Status Solidi (a) 211 (2014) 1928–1932, https://doi.org/10.1002/pssa.201330555.
[8] S. Yuvaraja, H. Faber, M. Kumar, N. Xiao, G.I. Maciel García, X. Tang, T. D. Anthopoulos, X. Li, Three-dimensional integrated metal-oxide transistors, Nat. Electron. 7 (2024) 768–776, https://doi.org/10.1038/s41928-024-01205-0.
[9] A.B.H. Tay, J.T.L. Thong, Fabrication of super-sharp nanowire atomic force microscope probes using a field emission induced growth technique, Rev. Sci. Instrum. 75 (2004) 3248–3255, https://doi.org/10.1063/1.1791321.
[10] C.K. Chan, H. Peng, G. Liu, K. McIlwrath, X.F. Zhang, R.A. Huggins, Y. Cui, High-performance lithium battery anodes using silicon nanowires, Nat. Nanotechnol. 3 (2008) 31–35, https://doi.org/10.1038/nnano.2007.411.
[11] S.K. Cheah, E. Perre, M. Rooth, M. Fondell, A. Harsta, L. Nyholm, M. Boman, T. Gustafsson, J. Lu, P. Simon, K. Edstrom, Self-supported three-dimensional nanoelectrodes for microbattery applications, Nano Lett. 9 (2009) 3230–3233, https://doi.org/10.1021/nl9014843.
[12] L. Mai, X. Tian, X. Xu, L. Chang, L. Xu, Nanowire electrodes for electrochemical energy storage devices, Chem. Rev. 114 (2014) 11828–11862, https://doi.org/10.1021/cr500177a.
[13] S.A. Ahad, T. Kennedy, H. Geaney, Si nanowires: from model system to practical Li-ion anode material and beyond, ACS Energy Lett. 9 (2024) 1548–1561, https://doi.org/10.1021/acsenergylett.4c00262.
[14] C. Pan, L. Dong, G. Zhu, S. Niu, R. Yu, Q. Yang, Y. Liu, Z.L. Wang, High-resolution electroluminescent imaging of pressure distribution using a piezoelectric nanowire LED array, Nat. Photonics 7 (2013) 752–758, https://doi.org/10.1038/nphoton.2013.191.
[15] J.T. Robinson, M. Jorgolli, A.K. Shalek, M.-H. Yoon, R.S. Gertner, H. Park, Vertical nanowire electrode arrays as a scalable platform for intracellular interfacing to neuronal circuits, Nat. Nanotechnol. 7 (2012) 180–184, https://doi.org/10.1038/nnano.2011.249.
[16] J. Qiu, J. Li, W. Li, K. Wang, S. Zhang, C.H. Suk, C. Wu, X. Zhou, Y. Zhang, T. Guo, T.W. Kim, Advancements in nanowire-based devices for neuromorphic computing: a review, ACS Nano 18 (2024) 31632–31659, https://doi.org/10.1021/acsnano.4c10170.
[17] Y. Qin, X. Wang, Z.L. Wang, Microfibre–nanowire hybrid structure for energy scavenging, nature 451 (2008) 809–813, https://doi.org/10.1038/nature06601.
[18] L. Xue, S.V. Savilov, V.V. Lunin, H. Xia, Self-standing porous LiCoO2 nanosheet arrays as 3D cathodes for flexible Li-ion batteries, Adv. Funct. Mater. 28 (2017), https://doi.org/10.1002/adfm.201705836.
[19] Q. Xia, M. Ni, M. Chen, H. Xia, Low-temperature synthesized self-supported single-crystalline LiCoO2 nanoflake arrays as advanced 3D cathodes for flexible lithium-ion batteries, J. Mater. Chem. A 7 (2019) 6187–6196, https://doi.org/10.1039/c9ta00351g.
[20] H. Xia, Y. Wan, W. Assenmacher, W. Mader, G. Yuan, L. Lu, Facile synthesis of chain-like LiCoO2 nanowire arrays as three-dimensional cathode for microbatteries, NPG Asia Mater. 6 (2014), https://doi.org/10.1038/am.2014.72 e126-e126.
[21] R.V. Salvatierra, A.R.O. Raji, S.K. Lee, Y. Ji, L. Li, J.M. Tour, Silicon nanowires and lithium cobalt oxide nanowires in graphene nanoribbon papers for full lithium ion battery, Adv. Energy Mater. 6 (2016), https://doi.org/10.1002/aenm.201600918.
[22] Q. Chen, J. Li, C. Liao, W. Liang, X. Lou, Z. Liu, J. Zhang, Y. Tang, L. Mai, L. Zhou, K. Amine, High mass loading potassium ion stabilized manganese dioxide

nanowire forests for rechargeable Zn batteries, Nano Energy 126 (2024), https://doi.org/10.1016/j.nanoen.2024.109607.
[23] L. Wang, J. Yan, Z. Xu, W. Wang, J. Wen, X. Bai, Rate mechanism of vanadium oxide coated tin dioxide nanowire electrode for lithium ion battery, Nano Energy 42 (2017) 294–299, https://doi.org/10.1016/j.nanoen.2017.10.059.
[24] Q. An, Y. Li, H. Deog Yoo, S. Chen, Q. Ru, L. Mai, Y. Yao, Graphene decorated vanadium oxide nanowire aerogel for long-cycle-life magnesium battery cathodes, Nano Energy 18 (2015) 265–272, https://doi.org/10.1016/j.nanoen.2015.10.029.
[25] Z.-S. Wu, G. Zhou, L.-C. Yin, W. Ren, F. Li, H.-M. Cheng, Graphene/metal oxide composite electrode materials for energy storage, Nano Energy 1 (2012) 107–131, https://doi.org/10.1016/j.nanoen.2011.11.001.
[26] G. Fang, J. Zhou, C. Liang, A. Pan, C. Zhang, Y. Tang, X. Tan, J. Liu, S. Liang, MOFs nanosheets derived porous metal oxide-coated three-dimensional substrates for lithium-ion battery applications, Nano Energy 26 (2016) 57–65, https://doi.org/10.1016/j.nanoen.2016.05.009.
[27] C. Shen, X. Gao, C. Chen, S. Ren, J.L. Xu, Y.D. Xia, S.D. Wang, ZnO nanowire optoelectronic synapse for neuromorphic computing, Nanotechnology 33 (2021), https://doi.org/10.1088/1361-6528/ac3687.
[28] Z. Kuncic, T. Nakayama, Neuromorphic nanowire networks: principles, progress and future prospects for neuro-inspired information processing, Adv. Phys. X 6 (2021), https://doi.org/10.1080/23746149.2021.1894234.
[29] T.-S. Kim, Y. Lee, W. Xu, Y.H. Kim, M. Kim, S.-Y. Min, T.H. Kim, H.W. Jang, T.-W. Lee, Direct-printed nanoscale metal-oxide-wire electronics, Nano Energy 58 (2019) 437–446, https://doi.org/10.1016/j.nanoen.2019.01.052.
[30] H. Zhou, An overview of hot carrier degradation on gate-all-around nanosheet transistors, Micromachines (Basel) 16 (2025), https://doi.org/10.3390/mi16030311.
[31] X. Xie, Y. Li, Z.Q. Liu, M. Haruta, W. Shen, Low-temperature oxidation of CO catalysed by Co(3)O(4) nanorods, Nature 458 (2009) 746–749, https://doi.org/10.1038/nature07877.
[32] Y. Zhang, A. Kolmakov, S. Chretien, H. Metiu, M. Moskovits, Control of catalytic reactions at the surface of a metal oxide nanowire by manipulating electron density inside it, Nano Lett. 4 (2004) 403–407, https://doi.org/10.1021/nl034968f.
[33] Y. Zhang, A. Kolmakov, Y. Lilach, M. Moskovits, Electronic control of chemistry and catalysis at the surface of an individual tin oxide nanowire, J. Phys. Chem. B 109 (2005) 1923–1929, https://doi.org/10.1021/jp045509l.
[34] C. Liu, J. Tang, H.M. Chen, B. Liu, P. Yang, A fully integrated nanosystem of semiconductor nanowires for direct solar water splitting, Nano Lett. 13 (2013) 2989–2992, https://doi.org/10.1021/nl401615t.
[35] J. Luo, L. Steier, M.K. Son, M. Schreier, M.T. Mayer, M. Gratzel, Cu2O Nanowire photocathodes for efficient and durable solar water splitting, Nano Lett. 16 (2016) 1848–1857, https://doi.org/10.1021/acs.nanolett.5b04929.
[36] G. Wang, H. Wang, Y. Ling, Y. Tang, X. Yang, R.C. Fitzmorris, C. Wang, J. Z. Zhang, Y. Li, Hydrogen-treated TiO2 nanowire arrays for photoelectrochemical water splitting, Nano Lett. 11 (2011) 3026–3033, https://doi.org/10.1021/nl201766h.
[37] X. Yang, A. Wolcott, G. Wang, A. Sobo, R.C. Fitzmorris, F. Qian, J.Z. Zhang, Y. Li, Nitrogen-doped ZnO nanowire arrays for photoelectrochemical water splitting, Nano Lett. 9 (2009) 2331–2336, https://doi.org/10.1021/nl900772q.
[38] X. Li, S.M. Dai, P. Zhu, L.L. Deng, S.Y. Xie, Q. Cui, H. Chen, N. Wang, H. Lin, Efficient perovskite solar cells depending on TiO2 nanorod arrays, ACS Appl. Mater. Interfaces 8 (2016) 21358–21365, https://doi.org/10.1021/acsami.6b05971.
[39] D.-Y. Son, J.-H. Im, H.-S. Kim, N.-G. Park, 11% Efficient perovskite solar cell based on ZnO nanorods: an effective charge collection system, J. Phys. Chem. C 118 (2014) 16567–16573, https://doi.org/10.1021/jp412407j.
[40] N. Bowler, Four-point potential drop measurements for materials characterization, Meas. Sci. Technol. 22 (2011), https://doi.org/10.1088/0957-0233/22/1/012001.
[41] F. Leonard, A.A. Talin, Electrical contacts to one- and two-dimensional nanomaterials, Nat. Nanotechnol. 6 (2011) 773–783, https://doi.org/10.1038/nnano.2011.196.
[42] A.A. Talin, F. Léonard, A.M. Katzenmeyer, B.S. Swartzentruber, S.T. Picraux, M. E. Toimil-Molares, J.G. Cederberg, X. Wang, S.D. Hersee, A. Rishinaramangalum, Transport characterization in nanowires using an electrical nanoprobe, Semicond. Sci. Technol. 25 (2010), https://doi.org/10.1088/0268-1242/25/2/024015.
[43] G. Binnig, H. Rohrer, Scanning tunneling microscopy—from birth to adolescence, Rev. Mod. Phys. 59 (1987) 615–625, https://doi.org/10.1103/RevModPhys.59.615.
[44] H.J. Zandvliet, A. van Houselt, Scanning tunneling spectroscopy, Annu. Rev. Anal. Chem. 2 (2009) 37–55, https://doi.org/10.1146/annurev-anchem-060908-155213.
[45] R.M. Feenstra, Band gap of the Ge(111)2×1 and Si(111)2×1 surfaces by scanning tunneling spectroscopy, Phys. Rev. B 44 (1991) 13791–13794, https://doi.org/10.1103/PhysRevB.44.13791.
[46] O. Gurlu, H.J. Zandvliet, B. Poelsema, Electronic properties of (2× 1) and c (4× 2) domains on Ge (001) studied by scanning tunneling spectroscopy, Phys. Rev. Lett. 93 (2004) 066101, https://doi.org/10.1103/PhysRevLett.93.066101.
[47] R.M. Feenstra, J. Lee, M. Kang, G. Meyer, K. Rieder, Band gap of the Ge (111) c (2× 8) surface by scanning tunneling spectroscopy, Phys. Rev. B 73 (2006) 035310, https://doi.org/10.1103/PhysRevB.73.035310.
[48] Y. Okada, Y. Ando, R. Shimizu, E. Minamitani, S. Shiraki, S. Watanabe, T. Hitosugi, Scanning tunnelling spectroscopy of superconductivity on surfaces of LiTi2O4(111) thin films, Nat. Commun. 8 (2017) 15975, https://doi.org/10.1038/ncomms15975.
[49] S. Wilfert, M. Schmitt, H. Schmidt, T. Mauerer, P. Sessi, H. Wang, Q. Mao, M. Fang, M. Bode, Scanning tunneling microscopy and spectroscopy studies of the heavy-electron superconductor TlNi2Se2, Phys. Rev. B 97 (2018), https://doi.org/10.1103/PhysRevB.97.014514.
[50] S. Zhu, L. Kong, L. Cao, H. Chen, M. Papaj, S. Du, Y. Xing, W. Liu, D. Wang, C. Shen, Nearly quantized conductance plateau of vortex zero mode in an iron-based superconductor, Science 367 (2020) 189–192, https://doi.org/10.1126/science.aax0274.
[51] S. Dan, S. Chatterjee, S. Paramanik, A.J. Pal, Necessity of quantifying urbach energy through scanning tunneling spectroscopy, J. Phys. Chem. Lett. 13 (2022) 1660–1667, https://doi.org/10.1021/acs.jpclett.1c03935.
[52] J. Tersoff, D.R. Hamann, Theory of the scanning tunneling microscope, Phys. Rev. B Condens. Matter 31 (1985) 805–813, https://doi.org/10.1103/physrevb.31.805.
[53] R.M. Feenstra, Scanning tunneling spectroscopy, Surf. Sci. 299-300 (1994) 965–979, https://doi.org/10.1016/0039-6028(94)90710-2.
[54] D. Bonnell, Scanning probe microscopy and spectroscopy: theory, techniques, and applications, John Wiley & Sons, 2000.
[55] M. Passoni, C.E. Bottani, Transfer Hamiltonian analytical theory of scanning tunneling spectroscopy, Phys. Rev. B 76 (2007), https://doi.org/10.1103/PhysRevB.76.115404.
[56] P.M. Williams, M.S. Cheema, M.C. Davies, D.E. Jackson, S.J.B. Tendler, Biological Applications of Scanning Tunneling Microscopy, in: C. Jones, B. Mulloy, A. H. Thomas (Eds.), Microscopy, Optical Spectroscopy, and Macroscopic Techniques, Humana Press, Totowa, NJ, 1994, pp. 25–37.
[57] E. Shapir, L. Sagiv, T. Molotsky, A.B. Kotlyar, R.D. Felice, D. Porath, Electronic structure of G4-DNA by scanning tunneling spectroscopy, J. Phys. Chem. C 114 (2010) 22079–22084, https://doi.org/10.1021/jp107952y.
[58] J.E. Hoffman, Spectroscopic scanning tunneling microscopy insights into Fe-based superconductors, Rep. Progress. Phys. 74 (2011), https://doi.org/10.1088/0034-4885/74/12/124513.
[59] J.-X. Yin, S.H. Pan, M. Zahid Hasan, Probing topological quantum matter with scanning tunnelling microscopy, Nat. Rev. Phys. 3 (2021) 249–263, https://doi.org/10.1038/s42254-021-00293-7.
[60] H. Feng, X. Xu, Y. Du, S.X. Dou, Application of scanning tunneling microscopy in electrocatalysis and electrochemistry, Electrochem. Energy Rev. 4 (2021) 249–268, https://doi.org/10.1007/s41918-020-00074-3.
[61] J. Wan, H.-J. Yan, R. Wen, L.-J. Wan, In situ visualization of electrochemical processes in solid-state lithium batteries, ACS Energy Lett. 7 (2022) 2988–3002, https://doi.org/10.1021/acsenergylett.2c01069.
[62] J.A. Kubby, J.E. Griffith, R.S. Becker, J.S. Vickers, Tunneling microscopy of Ge (001), Phys. Rev. B Condens. Matter 36 (1987) 6079–6093, https://doi.org/10.1103/physrevb.36.6079.
[63] R.M. Feenstra, J.A. Stroscio, A.P. Fein, Tunneling spectroscopy of the Si(111)2 × 1 surface, Surf. Sci. 181 (1987) 295–306, https://doi.org/10.1016/0039-6028(87)90170-1.
[64] R.J. Hamers, P. Avouris, F. Bozso, Imaging chemical-bond formation with the scanning tunneling microscope: NH3 dissociation on Si(001), Phys. Rev. Lett. 59 (1987) 2071–2074, https://doi.org/10.1103/PhysRevLett.59.2071.
[65] B. Voigtländer. Scanning probe microscopy: Atomic force microscopy and scanning tunneling microscopy, Springer, 2015, https://doi.org/10.1007/978-3-662-45240-0.
[66] P. Mårtensson, R. Feenstra, Geometric and electronic structure of antimony on the GaAs (110) surface studied by scanning tunneling microscopy, Phys. Rev. B 39 (1989) 7744, https://doi.org/10.1103/PhysRevB.39.7744.
[67] M. Prietsch, A. Samsavar, R. Ludeke, Structural and electronic properties of the Bi/GaP (110) interface, Phys. Rev. B 43 (1991) 11850, https://doi.org/10.1103/PhysRevB.43.11850.
[68] R.M. Feenstra, Tunneling spectroscopy of the (110) surface of direct-gap III-V semiconductors, Phys. Rev. B Condens. Matter 50 (1994) 4561–4570, https://doi.org/10.1103/physrevb.50.4561.
[69] C.J. Chen. Introduction to Scanning Tunneling Microscopy, 2nd ed, Oxford University Press, New York, NY, 2007, https://doi.org/10.1093/oso/9780198856559.001.0001.
[70] S.D. Mo, Y.N. Xu, W.Y. Ching, Electronic and structural properties of bulk γ-Al2O3, J. Am. Ceram. Soc. 80 (2005) 1193–1197, https://doi.org/10.1111/j.1151-2916.1997.tb02963.x.
[71] R.H. French, Electronic band structure of Al2O3, with comparison to alon and AlN, J. Am. Ceram. Soc. 73 (2005) 477–489, https://doi.org/10.1111/j.1151-2916.1990.tb06541.x.
[72] J. Olivier, R. Poirier, Electronic structure of Al2O3 from electron energy loss spectroscopy, Surf. Sci. 105 (1981) 347–356, https://doi.org/10.1016/0039-6028(81)90167-9.
[73] T.T. Song, M. Yang, J.W. Chai, M. Callsen, J. Zhou, T. Yang, Z. Zhang, J.S. Pan, D. Z. Chi, Y.P. Feng, S.J. Wang, The stability of aluminium oxide monolayer and its interface with two-dimensional materials, Sci. Rep. 6 (2016) 29221, https://doi.org/10.1038/srep29221.
[74] S.M. George, Atomic layer deposition: an overview, Chem. Rev. 110 (2010) 111–131, https://doi.org/10.1021/cr900056b.
[75] J.W. Elam, D. Routkevitch, P.P. Mardilovich, S.M. George, Conformal coating on ultrahigh-aspect-ratio nanopores of anodic alumina by atomic layer deposition, Chem. Mater. 15 (2003) 3507–3517, https://doi.org/10.1021/cm0303080.
[76] W.D. Oliver, P.B. Welander, Materials in superconducting quantum bits, MRS Bull. 38 (2013) 816–825, https://doi.org/10.1557/mrs.2013.229.

[77] X. Han, Y. Gong, K.K. Fu, X. He, G.T. Hitz, J. Dai, A. Pearse, B. Liu, H. Wang, G. Rubloff, Negating interfacial impedance in garnet-based solid-state Li metal batteries, Nat. Mater. 16 (2017) 572–579, https://doi.org/10.1038/nmat4821.

[78] H.-M. Cheng, F.-M. Wang, J.P. Chu, R. Santhanam, J. Rick, S.-C. Lo, Enhanced cycleabity in lithium ion batteries: resulting from atomic layer depostion of Al2O3 or TiO2 on LiCoO2 electrodes, J. Phys. Chem. C 116 (2012) 7629–7637, https://doi.org/10.1021/jp210551r.

[79] T. Feng, Y. Xu, Z. Zhang, X. Du, X. Sun, L. Xiong, R. Rodriguez, R. Holze, Low-cost Al2O3 coating layer as a preformed SEI on natural graphite powder to improve coulombic efficiency and high-rate cycling stability of lithium-ion batteries, ACS Appl. Mater. Interfaces 8 (2016) 6512–6519, https://doi.org/10.1021/acsami.6b00231.

[80] J.H. Woo, J.E. Trevey, A.S. Cavanagh, Y.S. Choi, S.C. Kim, S.M. George, K.H. Oh, S.-H. Lee, Nanoscale interface modification of LiCoO2 by Al2O3 atomic layer deposition for solid-state Li batteries, J. Electrochem. Soc. 159 (2012) A1120, https://doi.org/10.1149/2.085207jes.

[81] I.D. Scott, Y.S. Jung, A.S. Cavanagh, Y. Yan, A.C. Dillon, S.M. George, S.-H. Lee, Ultrathin coatings on nano-LiCoO2 for Li-ion vehicular applications, Nano Lett 11 (2011) 414–418, https://doi.org/10.1021/nl1030198.

[82] J.A. Stroscio, W.J. Kaiser, Scanning tunneling microscopy, Academic press, 1993.

[83] R.M. Feenstra, A prospective: quantitative scanning tunneling spectroscopy of semiconductor surfaces, Surf. Sci. 603 (2009) 2841–2844, https://doi.org/10.1016/j.susc.2009.08.002.

[84] E.O. Filatova, A.S. Konashuk, Interpretation of the changing the band gap of Al2O3 depending on its crystalline form: connection with different local symmetries, J. Phys. Chem. C 119 (2015) 20755–20761, doi:10.1021/acs.jpcc.5b06843.

[85] S. Toyoda, T. Shinohara, H. Kumigashira, M. Oshima, Y. Kato, Significant increase in conduction band discontinuity due to solid phase epitaxy of Al2O3 gate insulator films on GaN semiconductor, Appl. Phys. Lett. 101 (2012), https://doi.org/10.1063/1.4769818.

[86] C.M. Julien, A. Mauger, O.M. Hussain, Sputtered LiCoO(2) cathode materials for all-solid-state thin-film lithium microbatteries, Mater. (Basel) 12 (2019), https://doi.org/10.3390/ma12172687.

[87] T. Stockhoff, T. Gallasch, F. Berkemeier, G. Schmitz, Ion beam sputter-deposition of LiCoO2 films, Thin Solid. Films 520 (2012) 3668–3674, https://doi.org/10.1016/j.tsf.2011.12.065.

[88] S.J. Turrell, S. Zekoll, J. Liu, C.R.M. Grovenor, S.C. Speller, Optimization of a potential manufacturing process for thin-film LiCoO2 cathodes, Thin Solid. Films 735 (2021), https://doi.org/10.1016/j.tsf.2021.138888.

[89] M. Winter, B. Barnett, K. Xu, Before Li ion batteries, Chem. Rev. 118 (2018) 11433–11456, https://doi.org/10.1021/acs.chemrev.8b00422.

[90] X. Wang, X. Wang, Y. Lu, Realizing high voltage lithium cobalt oxide in lithium-ion batteries, Ind. Eng. Chem. Res. 58 (2019) 10119–10139, https://doi.org/10.1021/acs.iecr.9b01236.

[91] L. Wang, B. Chen, J. Ma, G. Cui, L. Chen, Reviving lithium cobalt oxide-based lithium secondary batteries-toward a higher energy density, Chem. Soc. Rev. 47 (2018) 6505–6602, https://doi.org/10.1039/c8cs00322j.

[92] E.J. Fuller, F.E. Gabaly, F. Leonard, S. Agarwal, S.J. Plimpton, R.B. Jacobs-Gedrim, C.D. James, M.J. Marinella, A.A. Talin, Li-ion synaptic transistor for low power analog computing, Adv. Mater. 29 (2017) 1604310, https://doi.org/10.1002/adma.201604310.

[93] E.J. Fuller, D.S. Ashby, C. Polop, E. Salagre, B. Bhargava, Y. Song, E. Vasco, J. D. Sugar, P. Albertus, T.O. Menteş, A. Locatelli, P. Segovia, M.Á. Gonzalez-Barrio, A. Mascaraque, E.G. Michel, A.A. Talin, Imaging phase segregation in nanoscale LixCoO2 single particles, ACS Nano 16 (2022) 16363–16371, https://doi.org/10.1021/acsnano.2c05594.

[94] A.A. Talin, Y. Li, D.A. Robinson, E.J. Fuller, S. Kumar, ECRAM materials, devices, circuits and architectures: a perspective, Adv. Mater. 35 (2023) 2204771, https://doi.org/10.1002/adma.202204771.

[95] A.A. Talin, J. Meyer, J. Li, M. Huang, M. Schwacke, H.W. Chung, L. Xu, E. J. Fuller, Y. Li, B. Yildiz, Electrochemical random-access memory: progress, perspectives, and opportunities, Chem. Rev. 125 (2025) 1962–2008, https://doi.org/10.1021/acs.chemrev.4c00512.

[96] W. Zhang, Y. Chen, C. Xu, C. Lin, J. Tao, Y. Lin, J. Li, O.V. Kolosov, Z. Huang, Tunable electrical field-induced metal-insulator phase separation in LiCoO2 synaptic transistor operating in post-percolation region, Nano Energy 108 (2023), https://doi.org/10.1016/j.nanoen.2023.108199.

[97] M. Ménétrier, I. Saadoune, S. Levasseur, C. Delmas, The insulator-metal transition upon lithium deintercalation from LiCoO2: electronic properties and 7Li NMR study, J. Mater. Chem. 9 (1999) 1135–1140, https://doi.org/10.1039/a900016j.

[98] C.A. Marianetti, G. Kotliar, G. Ceder, A first-order Mott transition in LixCoO2, Nat. Mater. 3 (2004) 627–631, https://doi.org/10.1038/nmat1178.

[99] H. Kang, J. Lee, T. Rodgers, J.-H. Shim, S. Lee, Electrical conductivity of delithiated lithium cobalt oxides: conductive atomic force microscopy and density functional theory study, J. Phys. Chem. C 123 (2019) 17703–17710, https://doi.org/10.1021/acs.jpcc.9b03232.

[100] N. Balke, S. Jesse, A.N. Morozovska, E. Eliseev, D.W. Chung, Y. Kim, L. Adamczyk, R.E. Garcia, N. Dudney, S.V. Kalinin, Nanoscale mapping of ion diffusion in a lithium-ion battery cathode, Nat. Nanotechnol. 5 (2010) 749–754, https://doi.org/10.1038/nnano.2010.174.

[101] N. Balke, S. Jesse, Y. Kim, L. Adamczyk, A. Tselev, I.N. Ivanov, N.J. Dudney, S. V. Kalinin, Real space mapping of Li-ion transport in amorphous Si anodes with nanometer resolution, Nano Lett. 10 (2010) 3420–3425, https://doi.org/10.1021/nl101439x.

[102] S. Jesse, N. Balke, E. Eliseev, A. Tselev, N.J. Dudney, A.N. Morozovska, S. V. Kalinin, Direct mapping of ionic transport in a Si anode on the nanoscale: time domain electrochemical strain spectroscopy study, ACS Nano 5 (2011) 9682–9695, https://doi.org/10.1021/nn203141g.

[103] T.M. Arruda, A. Kumar, S. Jesse, G.M. Veith, A. Tselev, A.P. Baddorf, N. Balke, S. V. Kalinin, Toward quantitative electrochemical measurements on the nanoscale by scanning probe microscopy: environmental and current spreading effects, ACS Nano 7 (2013) 8175–8182, https://doi.org/10.1021/nn4034772.

[104] J.M. Larson, S.C. Bharath, W.G. Cullen, J.E. Reutt-Robey, Scanning MWCNT-nanopipette and probe microscopy: Li patterning and transport studies, Small 11 (2015) 4946–4958, https://doi.org/10.1002/smll.201500999.

[105] J. Larson, A. Talin, A. Pearse, A. Kozen, J. Reutt-Robey, Innovative SPM probes for energy-storage science: MWCNT-nanopipettes to nanobattery probes, APS March Meeting Abstracts (2016) p. A46. 002.

[106] E. Strelcov, S.M. Yang, S. Jesse, N. Balke, R.K. Vasudevan, S.V. Kalinin, Solid-state electrochemistry on the nanometer and atomic scales: the scanning probe microscopy approach, Nanoscale 8 (2016) 13838–13858, https://doi.org/10.1039/c6nr01524g.

[107] J. Larson. Innovative scanning probe methods for energy storage science: Elucidating the physics of battery materials at the nano-to-microscale, 2017.

[108] J.M. Larson, E. Gillette, K. Burson, Y. Wang, S.B. Lee, J.E. Reutt-Robey, Pascalammetry with operando microbattery probes: sensing high stress in solid-state batteries, Sci. Adv. 4 (2018) eaas8927, https://doi.org/10.1126/sciadv.aas8927.

[109] L. Collins, Y. Liu, O.S. Ovchinnikova, R. Proksch, Quantitative electromechanical atomic force microscopy, ACS Nano 13 (2019) 8055–8066, https://doi.org/10.1021/acsnano.9b02883.

[110] E. Strelcov, C. Arble, H. Guo, B.D. Hoskins, A. Yulaev, I.V. Vlassiouk, N. B. Zhitenev, A. Tselev, A. Kolmakov, Nanoscale mapping of the double layer potential at the graphene-electrolyte interface, Nano Lett. 20 (2020) 1336–1344, https://doi.org/10.1021/acs.nanolett.9b04823.

[111] E.J. Fuller, E. Strelcov, J.L. Weaver, M.W. Swift, J.D. Sugar, A. Kolmakov, N. Zhitenev, J.J. McClelland, Y. Qi, J.A. Dura, A.A. Talin, Spatially resolved potential and Li-ion distributions reveal performance-limiting regions in solid-state batteries, ACS Energy Lett. 6 (2021) 3944–3951, https://doi.org/10.1021/acsenergylett.1c01960.

[112] K. Hata, Y. Shibata, H. Shigekawa, Fine electronic structure of the buckled dimers of Si(100) elucidated by atomically resolved scanning tunneling spectroscopy and bias-dependent imaging, Phys. Rev. B 64 (2001), https://doi.org/10.1103/PhysRevB.64.235310.

[113] K. Hata, T. Kimura, S. Ozawa, H. Shigekawa, How to fabricate a defect free Si (001) surface, J. Vac. Sci. Technol. A Vac. Surf. Films 18 (2000) 1933–1936, https://doi.org/10.1116/1.582482.

[114] H. Kim, C.-Y. Chou, J.G. Ekerdt, G.S. Hwang, Structure and properties of Li−Si alloys: a first-principles study, J. Phys. Chem. C 115 (2011) 2514–2521, https://doi.org/10.1021/jp1083899.

[115] I. Gonzalez, A.N. Sosa, A. Trejo, M. Calvino, A. Miranda, M. Cruz-Irisson, Lithium effect on the electronic properties of porous silicon for energy storage applications: a DFT study, Dalton Trans. 47 (2018) 7505–7514, https://doi.org/10.1039/c8dt00355f.

[116] D. Ma, Z. Cao, A. Hu, Si-based anode materials for Li-ion batteries: a mini review, Nanomicro Lett. 6 (2014) 347–358, https://doi.org/10.1007/s40820-014-0008-2.

[117] W.-F. Ren, Y. Zhou, J.-T. Li, L. Huang, S.-G. Sun, Si anode for next-generation lithium-ion battery, Curr. Opin. Electrochem. 18 (2019) 46–54, https://doi.org/10.1016/j.coelec.2019.09.006.

[118] J. van Elp, J.L. Wieland, H. Eskes, P. Kuiper, G.A. Sawatzky, F.M. de Groot, T. S. Turner, Electronic structure of CoO, Li-doped CoO, and LiCoO2, Phys. Rev. B Condens. Matter 44 (1991) 6090–6103, https://doi.org/10.1103/physrevb.44.6090.

[119] B. Andriyevsky, K. Doll, T. Jacob, Electronic and transport properties of LiCoO2, Phys. Chem. Chem. Phys. 16 (2014) 23412–23420, https://doi.org/10.1039/c4cp03052d.

[120] G.A. Wei, T.E. Haas, R.B. Goldner, Thin-films of lithium cobalt oxide, Solid. State Ion. 58 (1992) 115–122, https://doi.org/10.1016/0167-2738(92)90018-K.

[121] D. Ensling, A. Thissen, S. Laubach, P.C. Schmidt, W. Jaegermann, Electronic structure ofLiCoO2thin films: a combined photoemission spectroscopy and density functional theory study, Phys. Rev. B 82 (2010), https://doi.org/10.1103/PhysRevB.82.195431.

[122] P. Ghosh, S. Mahanty, M.W. Raja, R.N. Basu, H.S. Maiti, Structure and optical absorption of combustion-synthesized nanocrystalline LiCoO2, J. Mater. Res. 22 (2011) 1162–1167, https://doi.org/10.1557/jmr.2007.0157.

[123] G. Kresse, J. Hafner, Ab initio molecular dynamics for liquid metals, Phys. Rev. B 47 (1993) 558, https://doi.org/10.1103/PhysRevB.47.558.

[124] G. Kresse, J. Furthmüller, Efficient iterative schemes for ab initio total-energy calculations using a plane-wave basis set, Phys. Rev. B 54 (1996) 11169, https://doi.org/10.1103/PhysRevB.54.11169.

[125] P.E. Blöchl, Projector augmented-wave method, Phys. Rev. B 50 (1994) 17953, https://doi.org/10.1103/PhysRevB.50.17953.

[126] G. Kresse, D. Joubert, From ultrasoft pseudopotentials to the projector augmented-wave method, Phys. Rev. B 59 (1999) 1758, https://doi.org/10.1103/PhysRevB.59.1758.

[127] J.P. Perdew, K. Burke, M. Ernzerhof, Generalized gradient approximation made simple, Phys. Rev. Lett. 77 (1996) 3865, https://doi.org/10.1103/PhysRevLett.77.3865.

[128] S.L. Dudarev, G.A. Botton, S.Y. Savrasov, C. Humphreys, A.P. Sutton, Electron-energy-loss spectra and the structural stability of nickel oxide: an LSDA+ U study, Phys. Rev. B 57 (1998) 1505, https://doi.org/10.1103/PhysRevB.57.1505.
[129] L. Wang, T. Maxisch, G. Ceder, Oxidation energies of transition metal oxides within the GGA+ U framework, Phys. Rev. B-Condens. Matter Mater. Phys. 73 (2006) 195107, https://doi.org/10.1103/PhysRevB.73.195107.
[130] M. Aykol, C. Wolverton, Local environment dependentGGA+Umethod for accurate thermochemistry of transition metal compounds, Phys. Rev. B 90 (2014), https://doi.org/10.1103/PhysRevB.90.115105.
[131] F. Zhou, M. Cococcioni, C.A. Marianetti, D. Morgan, G. Ceder, First-principles prediction of redox potentials in transition-metal compounds withLDA+U, Phys. Rev. B 70 (2004), https://doi.org/10.1103/PhysRevB.70.235121.
[132] K. Momma, F. Izumi, VESTA 3 for three-dimensional visualization of crystal, volumetric and morphology data, Appl. Crystallogr. 44 (2011) 1272–1276, https://doi.org/10.1107/S0021889811038970.
[133] C.H. Chen, C.T. Lin, Y.H. Lee, K.K. Liu, C.Y. Su, W. Zhang, L.J. Li, Electrical probing of submicroliter liquid using graphene strip transistors built on a nanopipette, Small 8 (2012) 43–46, https://doi.org/10.1002/smll.201101859.
[134] D. Golberg, P.M.F.J. Costa, M. Mitome, S. Hampel, D. Haase, C. Mueller, A. Leonhardt, Y. Bando, Copper-filled carbon nanotubes: rheostatlike behavior and femtogram copper mass transport, Adv. Mater. 19 (2007) 1937–1942, https://doi.org/10.1002/adma.200700126.
[135] K. Svensson, H. Olin, E. Olsson, Nanopipettes for metal transport, Phys. Rev. Lett. 93 (2004) 145901, https://doi.org/10.1103/PhysRevLett.93.145901.
[136] T.J. Boerner, S. Deems, T.R. Furlani, S.L. Knuth, J. Towns, Access: Advancing innovation: Nsf`s advanced cyberinfrastructure coordination ecosystem: Services & support, in: Practice and experience in advanced research computing 2023: Computing for the common good, 2023, pp. 173-176.



Gavin Gallop is currently a Ph.D. candidate in the Chemistry and Biochemistry department at Baylor University, under the supervision of Prof. Jonathan Larson. He received his B.S. degree in Chemistry from the University of Mary Hardin-Baylor in 2023. His research interests are scanning-probe characterization techniques relevant to energy storage materials and devices, with a particular interest in advancing methodologies for nanoscale interfacial characterization, including I-STS, s-SNOM, and nano-FTIR.



Ericsson McDermott received his B.S. degree in 2024 in Applied Mathematics from Evangel University, Springfield, MO. He is currently a Chemistry & Biochemistry Ph.D student at Baylor University in the Physical Chemistry division working in the lab of Prof. Jonathan Larson. His research focuses on applying mathematical and computational methods to further quantitative data interpretation of advanced scanning probe microscopies and spectroscopies – especially s-SNOM and nano-FTIR.



Puja Rijal is a Ph.D. candidate in the Department of Chemistry and Biochemistry at Baylor University and earned a B.S. in Biochemistry from Texas Woman's University. Research interests include computational chemistry, materials science, and theoretical approaches for understanding the structure and properties of functional materials and chemical systems. Current work focuses on the computational design and investigation of advanced materials for sustainable technologies, including applications in energy storage, electronic devices, and next-generation memory materials. Outside the lab, Puja enjoys traveling, hiking, kayaking, painting, and gardening, along with spending quality time with family.



Alexander C. Kozen is an Assistant Professor and Graduate Program Director in the department of Physics at the University of Vermont in Burlington, VT, USA. Professor Kozen's research group focuses on the nexus of thin film deposition, solid state ionics, and ultra-high vacuum surface science. Their work focuses on understanding the processing-structure-properties relationship of compositionally complex thin-film ion-conductive materials using advanced surface science and optical techniques to improve sustainability. They utilize approaches ubiquitous in the semiconductor industry to develop test platforms designed to elucidate fundamental properties of materials & interfaces for advanced solid-state batteries, solar cells, and next-generation computing. Professor Kozen has co-authored over 50 peer-reviewed publications and holds 1 U.S. Patent.



A. Alec Talin is a Distinguished Member of Technical Staff in the Materials Physics Department at Sandia National Laboratories and an Adjunct Associate Professor of Materials Science and Engineering at the University of Maryland, College Park. Alec earned a B.A. degree in Chemistry (1989) from UC San Diego and a Ph.D. in Materials Science and Engineering (1995) from UC Los Angeles. His research focuses on nanoionics and nanoelectronics for emerging computing and memory, solid state energy storage, photocatalytic and photoelectrocatalytic processes for solar fuels, and coordination polymers and metal organic frameworks for emerging electronics and energy applications.



Janice Reutt-Robey is Professor Emerita in the Department of Chemistry and Biochemistry at the University of Maryland. Janice earned a B.S. in Chemistry (1980) from Haverford College and a Ph.D. in Physical Chemistry (1986) from UC Berkeley. Her research is focused on the formation of chemical interfaces and nanostructures with targeted electronic and chemical properties for application in energy production and storage and nanotechnology. This includes directed assembly of molecular semiconductors, polymorph control in functionalized organic molecules, symmetry-breaking adsorbates in graphene, energy-storing nanostructures, and organic nano-photovoltaics for solar energy applications.



Kevin L. Shuford is a Full Professor and Associate Chair in the Department of Chemistry and Biochemistry at Baylor University in Waco, TX. An overarching theme in his research group is to utilize computational approaches to provide significant new insight into fundamental science problems that reside at the interface of chemistry, physics, and materials science. Research interests include low-dimensional materials, electronic structure theory, ultrafast quantum dynamics of molecules and semiconductors, noncovalent interactions, catalysis, light-driven processes, nano-optics, and plasmonics. An ongoing group focus is sustainability – specifically energy generation and storage. In the interstices, Shuford enjoys reading, traveling, sports, music and theatre.



Jonathan M. Larson is an Assistant Professor of Chemistry and Biochemistry at Baylor University and Affiliate Faculty in the Energy Technologies and Systems Division at Lawrence Berkeley National Laboratory (LBNL). He earned his Ph.D. in Physics from the University of Maryland, where he developed advanced scanning-probe methodologies to investigate energy materials at the nanoscale. During his postdoctoral research at LBNL, he expanded near-field imaging and nanoscale Fourier transform infrared spectroscopy (nano-FTIR) to electrochemical solid–liquid and solid–solid interfaces. His research focuses on developing and applying nanoscale spectroscopic tools to elucidate physicochemical phenomena governing electrochemically active materials and interfaces.